Quantum-Enhanced Support Vector Regression for Full-Duplex Self-Interference Cancellation

Mohamed Elsayed, *Member, IEEE,* and Octavia A. Dobre, *Fellow, IEEE*

***Abstract*—This letter proposes a quantum-enhanced support vector regression (QSVR) approach to cancel the self-interference in full-duplex transceivers. The proposed approach leverages quantum feature maps, incorporating quantum circuits, to encode classical data into a higher-dimensional feature space. Simulation results unveil a substantial performance enhancement by the proposed QSVR approach over the classical SVR and state-of-the-art hybrid quantum-classical neural network in the literature when being trained with a smaller set of training data.**

***Index Terms*—Quantum computing (QC), quantum-enhanced support vector regression (QSVR), quantum feature maps, full-duplex (FD) transceivers, self-interference cancellation (SIC).**

I. Introduction

FULL-DUPLEX (FD), promising a dual increase in spectral efficiency by enabling bidirectional communication between terminals in the same frequency band, is expected to be a cornerstone of the next-generation of wireless systems [1], [2]. This promise is, however, conditioned on integrating FD transceivers with effective self-interference cancellation (SIC) techniques, which are traditionally implemented in analog, propagation, or digital domains. Traditional SIC techniques have the potential of efficiently suppressing the self-interference (SI) at the receiver side; however, they come with a typical downside of requesting extra hardware, memory, and/or computational resources [3].

With the rapid pace of advancement in deep learning, machine learning (ML) approaches have expanded their frontiers to the SIC problem to replace traditional approaches, providing similar/better SIC performance accompanied by a reduction in the hardware, memory, and/or computational resources [3]-[10]. Specifically, classical support vector regression (SVR) has demonstrated superior performance advantages over traditional approaches when applied to SIC, with relatively small datasets, as reported in [8]-[10].

Quantum computing (QC), manipulating quantum mechanics for information processing, has recently garnered significant attention from both industrial and academic experts due to its potential to surpass classical computing in various disciplines, spanning finance, drug discovery, and computational chemistry [11]. QC also offers substantial opportunities to address challenging optimization problems in wireless communications, such as resource allocation, channel assignment, and task offloading [12], [13]. In classical computing, a classical bit can exist in one of two binary states, 0 or 1. Conversely, in QC, a quantum bit (qubit) can exist in a superposition of the two states simultaneously as $\psi = \alpha\left|0\right\rangle + \beta\left|1\right\rangle$, with $\left|.\right\rangle$ as the ket notation, whilst $\alpha, \beta \in \mathbb{C}$ refer to complex numbers and their magnitudes represent the probability of a qubit being in either state $\left|0\right\rangle$ or $\left|1\right\rangle$, with $\left|\alpha\right|^2 + \left|\beta\right|^2 = 1$ [14]. Stated differently, a register with b bits in a classical computer can only represent one of the 2^b possible combinations at a given time. On the other hand, a quantum register can simultaneously maintain a superposition of all 2^b states, enabling powerful parallel processing capabilities [12].

Quantum ML (QML), integrating QC with ML, has also progressed rapidly in recent years due to its potential advantages over classical ML methods. Rooted in the fundamentals of quantum mechanics, such as entanglement and superposition, QML can efficiently handle complex non-linear relationships that classical ML might struggle to solve [15]. Besides, QML has the potential to outperform classical ML in certain computational tasks, often with fewer training samples.

Inspired by the potential of QML to handle complex non-linear relationships with fewer training samples, this letter proposes a quantum-enhanced SVR (QSVR) approach for SIC in FD transceivers. The proposed approach leverages quantum feature maps, incorporating quantum circuits, to encode classical data into a higher-dimensional feature space. The encoded/transformed data is then integrated with a classical SVR to estimate the SI signal's non-linear component. Simulation results reveal a substantial performance enhancement by the proposed QSVR over the classical SVR and state-of-the-art hybrid quantum-classical neural network (NN) in the literature [15] when a small dataset is employed for the training process.

The remainder of this letter is organized as follows. Section II introduces a general FD transceiver system model. Section III details the proposed QSVR approach. Section IV presents numerical simulations, and Section V draws the conclusion.

II. System Model

Consider a general FD system model where an FD transceiver is incorporated with two stages of digital SIC, as depicted in Fig. 1. After being affected by various non-linear distortions within the transceiver and the SI channel, the received signal can be represented as [3]-[7]

$$y\left(n\right) = y_{SI}\left(n\right) + y_{SoI}\left(n\right) + \sigma\left(n\right), \tag{1}$$

with $\sigma\left(n\right) \sim \mathcal{CN}\left(0, \lambda^2\right)$ denoting the thermal noise, which follows the Gaussian distribution with zero mean and variance λ^2. $y_{SoI}\left(n\right)$ indicates the signal of interest from any FD terminal and $y_{SI}\left(n\right)$ represents the SI signal, defined as [3]-[7]

$$y_{SI}(n) = \sum_{\substack{p=1,\\ p\,odd}}^{P} \sum_{q=0}^{p} \sum_{m=0}^{M_i-1} h_{p,q}\left(m\right)\, x\left(n-m\right)^q x^*\left(n-m\right)^{p-q}, \tag{2}$$

with $(.)^*$ denoting the complex conjugate operator, $h_{p,q}\left(m\right)$ corresponding to a channel incorporating the non-linear distortions of the transceiver, M_i representing the memory length,

This work was supported by the Natural Sciences and Engineering Research Council of Canada (NSERC) through its Discovery Program and the Canada Research Chairs Program under Grant CRC-2022-00187.

Mohamed Elsayed and Octavia A. Dobre are with the Faculty of Engineering and Applied Science, Memorial University, NL A1B 3X5 St. John's, Canada, (e-mail: {memselim, odobre}@mun. ca). Mohamed Elsayed is also with the Faculty of Engineering, Sohag University, Sohag 82524, Egypt.

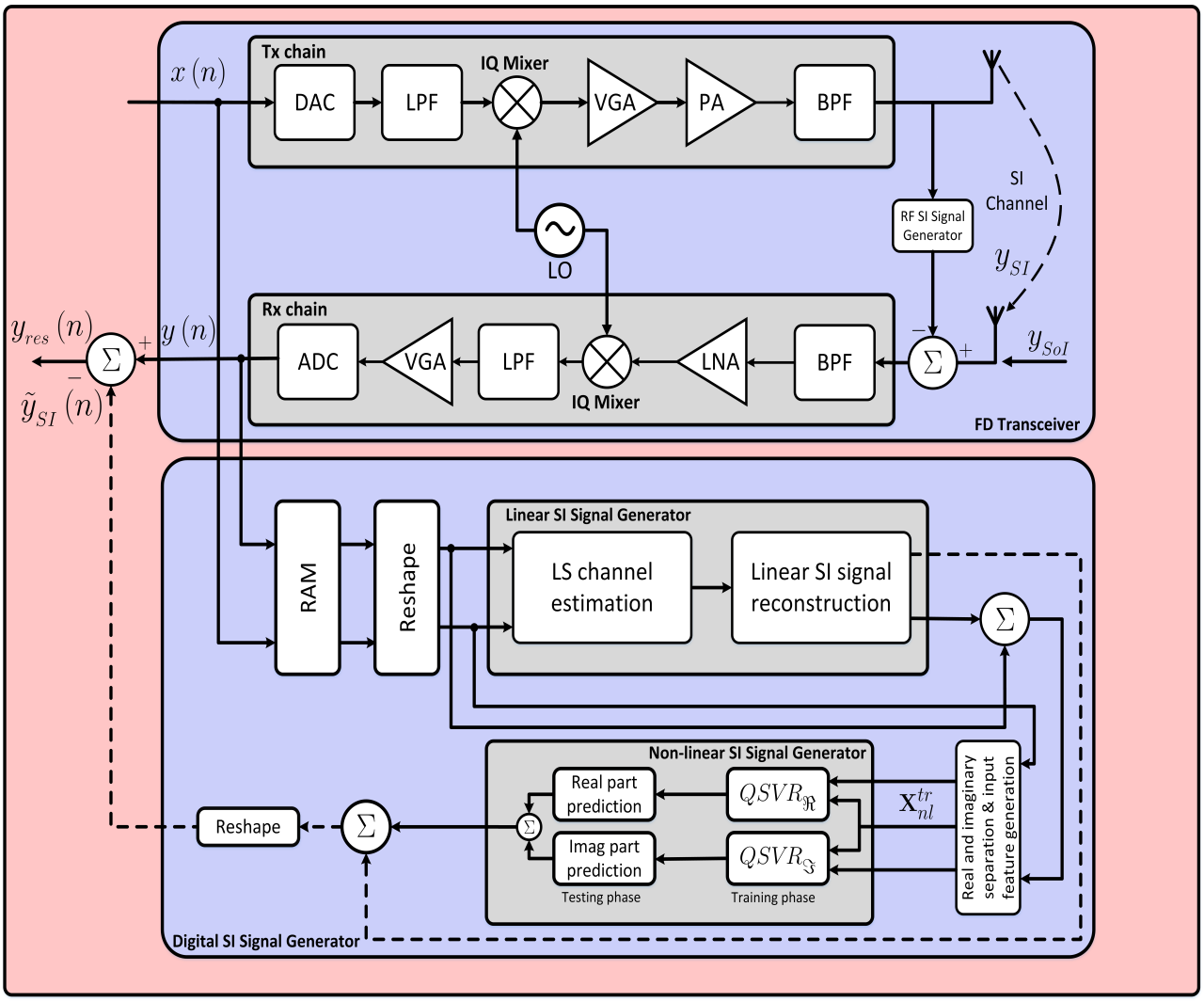

Fig. 1: FD transceiver [3], integrated with a non-linear SIC stage based on the proposed QSVR.

P indicating the non-linearity order of the power amplifier, and $x(n)$ referring to the n^{th} digital baseband input sample.

Assuming no signal of interest from any FD terminal, the primary objective of the digital SIC generator is to approximate the SI signal $y_{SI}(n)$, and construct its estimate $\widetilde{y}_{SI}(n)$ [3]-[7]. This can be achieved by applying both linear and non-linear digital SIC stages, as illustrated in Fig. 1. The former performs the linear digital SIC based on the widely used least-squares channel estimation, whilst the latter executes the non-linear digital SIC based on the proposed QSVR approach.

The total SIC, encompassing linear and non-linear SIC, can be assessed over a number of testing samples N as follows:

$$\mathcal{C}_{dB} = 10\log_{10}\left(\frac{\sum_{n=1}^{N}|y(n)|^2}{\sum_{n=1}^{N}|y_{res}(n)|^2}\right), \tag{3}$$

where $y_{res}(n)$ represents the residual SI signal after applying the two stages of digital cancellation, as depicted in Fig. 1.[1]

III. Proposed Quantum-Enhanced Support Vector Regression (QSVR)

The proposed QSVR, combining QC with classical SVR, is illustrated in Fig. 2. The classical data is first mapped/encoded from its original space to a higher-dimensional Hilbert space using a feature map. This feature map encodes classical data into quantum states via a quantum circuit [16], [17]. Once the data is mapped into the quantum space, a quantum kernel, offering a richer representation than classical kernels, is applied by computing the inner product of the encoded quantum states as

$$\kappa(\mathbf{x},\mathbf{x}') = \left|\langle\psi(\mathbf{x})|\psi(\mathbf{x}')\rangle\right|^2, \tag{4}$$

where $\psi(\mathbf{x})$ and $\psi(\mathbf{x}')$ refer to the quantum states obtained by encoding the input vectors, $\mathbf{x}$ and $\mathbf{x}'$, in the original input space by the parameterized quantum circuit in the feature map, whilst $\langle.|$ and $|.|$ denote the bra and absolute operators, respectively. After computing the quantum kernel, the quantum states are projected back to the classical space through quantum measurement, producing classical values serving as inputs for the subsequent classical SVR algorithm. It is worth noting that we employ two classical SVR algorithms, enhanced with two quantum kernels, to estimate the real and imaginary parts of the non-linear SI signal separately, as depicted in Fig. 1. These are denoted as $QSVR_{\Re}$ and $QSVR_{\Im}$, respectively. The input matrix $\mathbf{X}_{nl}^{tr}$ used to train the $QSVR_{\Re}$ and $QSVR_{\Im}$ is given by (5), with $\Re(u)$ and $\Im(u)$ referring to the

[1] A detailed description of the FD transceiver in Fig. 1 is provided in [3].

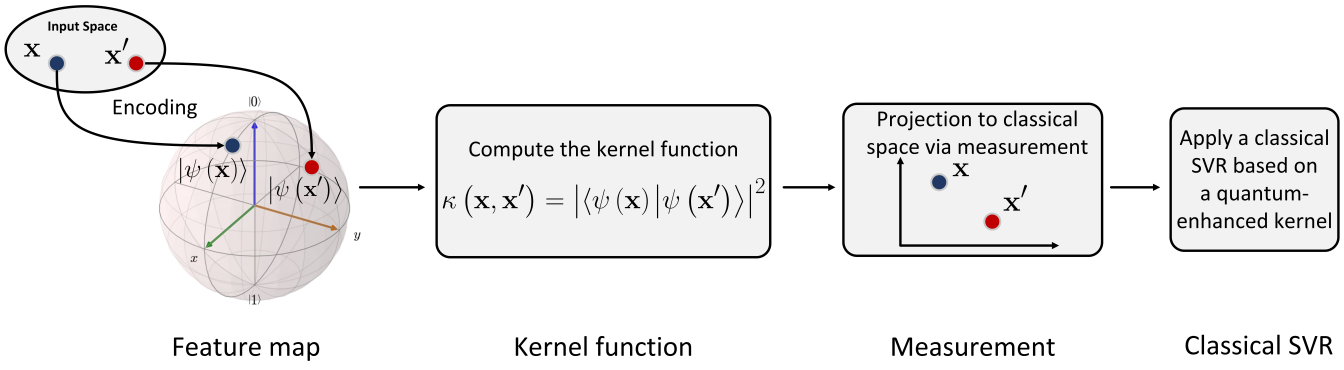

Fig. 2: Proposed QSVR approach.

real and imaginary parts of a variable u, respectively, and N_{tr} denoting the number of training samples. $\mathbf{x}_n = [\Re\{x(n)\} \ldots \Re\{x(n-M_i+1)\} \ \Im\{x(n)\} \ \ldots \ \Im\{x(n-M_i+1)\}]$ represents a row vector of this training matrix, which is utilized to construct the corresponding quantum state, $|\psi(\mathbf{x}_n)\rangle$, using the feature map.

This work explores various feature maps, such as the Pauli (e.g., Pauli-X, Pauli-Y, Pauli-Z) and the ZZ feature maps. The details of each are discussed in the following subsections.

A. Pauli Feature Map

1) Pauli-X feature map: The quantum circuit of the Pauli-X feature map is depicted in Fig. 3a. As shown, the Pauli-X feature map begins with a set of Hadamard gates applied to each of the qubits, $q_1 \cdots q_l$, creating superposition states to enable quantum parallelism, with l as the number of qubits. Each qubit then undergoes an x-rotational gate, $R_x(\alpha_i x_j)$, positioned between two other Hadamard gates, with x_j denoting the j^{th} input feature and α_i, $i \in \{\Re, \Im\}$, representing a rotation factor, which scales the angles of rotational gates helping to adjust the feature map and mitigate the overfitting [17].[2] It is important to note that the Pauli-X feature map does not involve any entanglement operations, as shown in Fig. 3a.

2) Pauli-Y feature map: The quantum circuit of the Pauli-Y feature map is depicted in Fig. 3b. Like the Pauli-X feature map, the Pauli-Y feature map applies a set of Hadamard gates to each qubit to create superposition states and enable quantum parallelism. A y-rotational gate between a $\frac{\pi}{2}$ x-rotational gate and its inverse is then applied to each qubit. It is quite apparent that the Pauli-Y feature map does not involve any entanglement operations, similar to the Pauli-X feature map.

3) Pauli-Z feature map: The quantum circuit of the Pauli-Z feature map is depicted in Fig. 3c. As observed, the Pauli-Z feature map employs a simple circuit that applies a Hadamard gate followed by a z-rotational gate to each qubit. It does not involve entanglement as the Pauli-X and Pauli-Y feature maps.

B. ZZ Feature Map

The quantum circuit of the ZZ feature map is depicted in Fig. 4. First, a set of Hadamard and z-rotational gates is applied to each qubit. Then, for every pair of qubits, $g, k \in \{1, \cdots l\}$,

[2]The rotation factors, $\alpha_\Re$ and $\alpha_\Im$, are respectively utilized in $QSVR_\Re$ and $QSVR_\Im$ to estimate the real and imaginary parts of the non-linear SI signal.

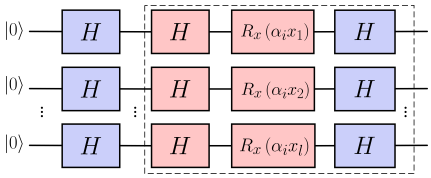

(a) Pauli-X feature map.

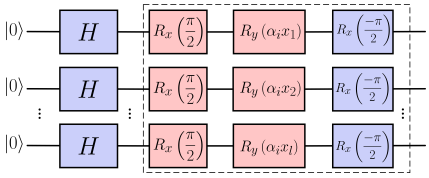

(b) Pauli-Y feature map.

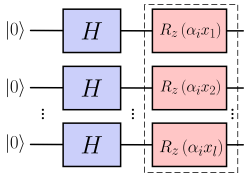

(c) Pauli-Z feature map.

Fig. 3: Pauli feature maps, with a rotation factor α_i, $i \in \{\Re, \Im\}$.

and $g < k$, a controlled-NOT (CNOT) gate is applied on qubit k and controlled by qubit g. The CNOT gates create quantum entanglement between qubits, enhancing the expressivity of the quantum circuit. Upon entangling the qubits, a rotation of $R_z(2(\pi - x_g)(\pi - x_k))$ is performed on qubit k. This is followed by repeating the process of applying a CNOT gate between the g^{th} and k^{th} qubits, as can be seen from Fig. 4.

It is worth mentioning that using a quantum feature map is required for both the training and inference stages of the QSVR. Thus, for real-time FD communication, each base station would need either an embedded quantum processor or access to a remote quantum processor, both of which can be challenging given the current limitations of available quantum hardware. An efficient solution is to simulate/approximate the quantum feature map during the inference stage until a breakthrough in the quantum hardware takes place. This simulation/approximation can be feasible and computationally efficient, especially if a small number of qubits is involved.

IV. Simulation Results

This section validates the performance of the proposed QSVR compared to the classical SVR, trained by the same input matrix in (5), but by employing a radial basis function (RBF) kernel instead of a quantum-enhanced kernel. The proposed method's performance is also validated against the recently introduced hybrid quantum-classical NN in [15], namely CNN-QLSTM. The following subsections detail the training dataset, simulation setup, and achieved results, respectively.

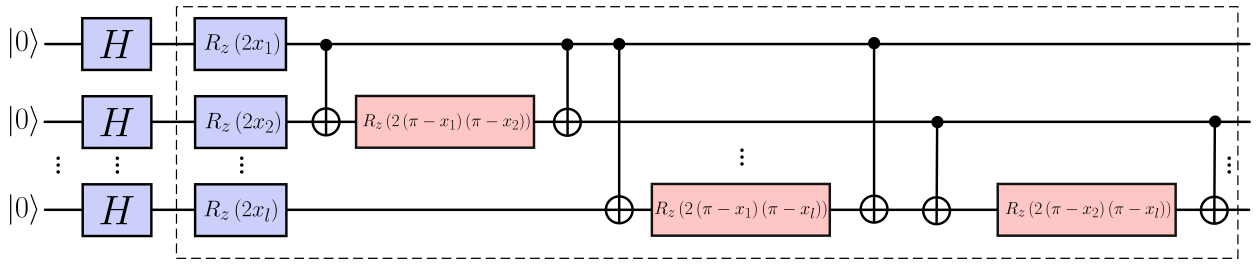

Fig. 4: ZZ feature map.

$$\mathbf{X}_{nl}^{tr} = \begin{bmatrix} \Re\{x(n)\} & \dots & \Re\{x(n-M_i+1)\} & \Im\{x(n)\} & \dots & \Im\{x(n-M_i+1)\} \\ \Re\{x(n+1)\} & \dots & \Re\{x(n-M_i+2)\} & \Im\{x(n+1)\} & \dots & \Im\{x(n-M_i+2)\} \\ \vdots & \vdots & \ddots & \ddots & \vdots & \vdots \\ \Re\{x(n+N_{tr}-M_i-1)\} & \dots & \Re\{x(n+N_{tr}-2M_i)\} & \Im\{x(n+N_{tr}-M_i-1)\} & \dots & \Im\{x(n+N_{tr}-2M_i)\} \end{bmatrix}, \tag{5}$$

A. Training Dataset

A real-time FD testbed is utilized to capture the training dataset by generating an orthogonal frequency division multiplexing signal, modulated by a quadrature phase shift keying, transmitted over 20 MHz bandwidth, and sampled at 80 MHz [7]. The average transmit power is adjusted to 32 dBm, the carrier frequency is set to 2.45 GHz, and the analog cancellation is tuned to 65 dB.[3] With this setup, a small dataset of 100 samples is obtained, with 90% allocated for training and 10% for testing.[4] After data collection, a classical computer is equipped with Qiskit and Scikit-Learn packages to train the proposed QSVR and compare its performance with the classical SVR and the recently introduced CNN-QLSTM [15].

B. Simulation Setup

Extensive tuning is conducted using a grid search to optimize the simulation parameters of the proposed QSVR. For both QSVR and SVR, we set the regularization terms to $C_{\Re} = C_{\Im} = 2$, the margin parameters to $\epsilon_{\Re} = \epsilon_{\Im} = 0.01$, and the memory length to $M_i = 3$. The gamma parameters of the RBF kernel adopted in the classical SVR are set to $\gamma_{\Re} = \gamma_{\Im} = 0.5$, whilst the number of qubits of the QSVR is chosen as $l = 2M_i = 6$. It is worth noting that for the CNN-QLSTM, we utilized the same setup in [15]. The following subsections analyze the effect of varying the feature map and rotation factors on the proposed QSVR performance.[5]

1) Effect of varying the feature map: Fig. 5 illustrates the effect of varying the feature map on the SIC performance of the proposed QSVR. As shown, the Pauli-Y and Pauli-Z feature maps result in the highest SIC performance. Subsequently, the Pauli-Z feature map is adopted for the proposed QSVR approach due to its straightforward quantum circuit implementation. It is worth noting that the ZZ feature map exhibits lower SIC performance, suggesting that complex entanglement is unnecessary and only a simple, non-entangled feature map suffices to model the SIC problem properly.

[3]As reported in [7], applying 65 dB total analog cancellation between the transmitter and receiver ensures that the generated dataset is not obtained in a regime that is limited by the transmitter or receiver quantization noise.

[4]Applying 0.9/0.1 train/test split is found to attain the best SIC performance.

[5]Using symmetric values for $C_{\Re}, C_{\Im}$, $\epsilon_{\Re}$, and $\epsilon_{\Im}$ of the proposed QSVR results in the optimal SIC performance; however, this does not extend to the rotation factors, $\alpha_{\Re}$ and $\alpha_{\Im}$, as will be discussed in the following subsection.

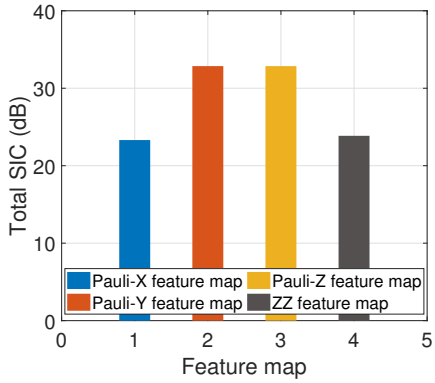

Fig. 5: Effect of varying the feature map on the SIC performance of the proposed QSVR.

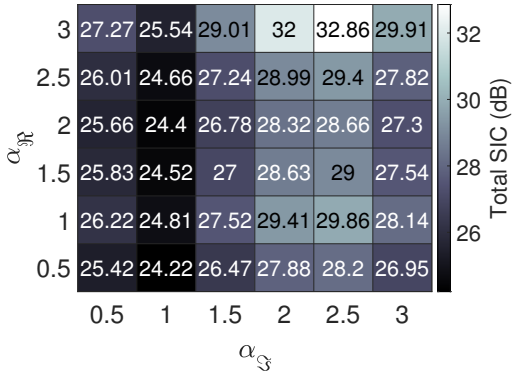

Fig. 6: Effect of varying the rotation factors, $\alpha_{\Re}$ and $\alpha_{\Im}$, on the SIC performance of the proposed QSVR.

2) Effect of varying the rotation factors: The effect of varying the rotation factors, $\alpha_{\Re}$, $\alpha_{\Im}$, of the Pauli-Z feature map on the SIC performance of the proposed QSVR is illustrated using the heatmap in Fig. 6. As shown, employing equal values for $\alpha_{\Re}$ and $\alpha_{\Im}$ does not necessarily yield the best SIC performance. Instead, deploying asymmetric values for the rotation factors, e.g., $\alpha_{\Re} = 3$ and $\alpha_{\Im} = 2.5$, results in the highest SIC performance, as can be observed from Fig. 6.

C. Achieved Results

1) Prediction capability: Fig. 7a depicts the prediction capability of the proposed QSVR, incorporating the Pauli-Z feature map, compared to the classical SVR and the recently

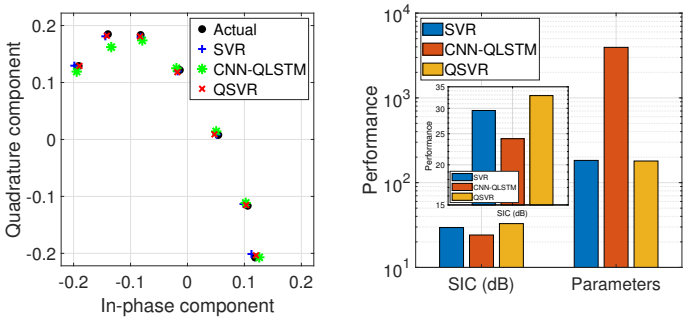

(a) Prediction capability. (b) SIC & trainable parameters.

Fig. 7: Performance of the proposed QSVR compared to the classical SVR and the recently introduced CNN-QLSTM [15].

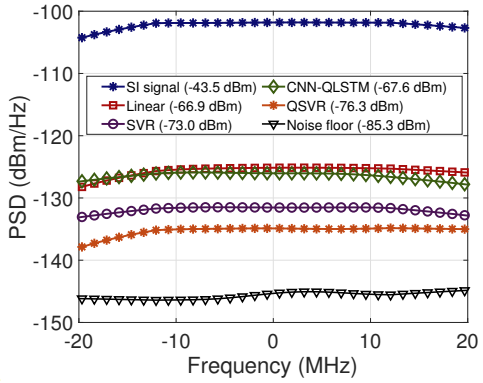

Fig. 8: PSD of the SI signal estimated by the proposed QSVR compared to the classical SVR and the recently introduced CNN-QLSTM [15].

introduced CNN-QLSTM [15]. As illustrated, the predicted values by the proposed QSVR closely align with the actual values, demonstrating a high prediction capability. In contrast, the classical SVR and the CNN-QLSTM predictions exhibit some deviations from the actual values, indicating a lower prediction capability and, subsequently, a degraded SIC performance, as will be discussed in the following subsection.

2) Total SIC and trainable parameters: Fig. 7b depicts the total SIC and the number of trainable parameters of the aforementioned SI cancelers. As shown, the proposed QSVR achieves a significantly higher SIC performance than the classical SVR while requiring comparable trainable parameters. The CNN-QLSTM conversely exhibits much lower SIC and even requires more trainable parameters as a result of being trained using a smaller set of data. It is worth mentioning that the performance improvement provided by the proposed QSVR comes from employing a quantum feature map rather than a classical feature map, i.e., a classical kernel. Applying quantum feature maps, i.e., quantum-enhanced kernels, enables mapping the input data into a higher-dimensional Hilbert feature space, making the data easier to fit—in some tasks—than it was in the case of being transformed using classical kernels. It is also worth mentioning that the proposed QSVR is highly effective in small-data regimes, while the CNN-QLSTM [15] is better suited for large-data scenarios.

3) Power spectral density (PSD) performance: Fig. 8 depicts the PSD of the SI signal estimated by different SI cancelers over a frequency range of -20 MHz to 20 MHz. As illustrated, the linear canceler reduces the SI signal's power from -43.5 dBm to -66.9 dBm, showing an effort in mitigating the SI. A slight improvement is then observed with CNN-QLSTM, which lowers the SI power to -67.6 dBm. A more remarkable reduction is achieved with the classical SVR, reaching an SI power of -73.0 dBm. Finally, the proposed QSVR provides the most significant enhancement, reducing the SI power to -76.3 dBm and approaching the noise floor power level. It is interesting to note that, unlike in [3]-[7], [15], the SI signal remains relatively flat across the entire frequency range. This behavior is attributed to the limited number of samples utilized to estimate the PSD curves in this study versus those employed in [3]-[7], [15].

V. Conclusion

This letter explored the feasibility of QSVR, leveraging quantum feature maps and incorporating quantum circuits, to cancel the SI in FD transceivers. The quantum feature maps enhanced the modeling accuracy by mapping classical data into a higher-dimensional Hilbert feature space. Simulation results validated the superiority of the proposed QSVR approach by achieving a higher SIC without additional parameters compared to the classical SVR and the hybrid quantum-classical NN in the literature when trained using a smaller set of data.

References

[1] B. Smida et al., "Full-duplex wireless for 6G: Progress brings new opportunities and challenges," *IEEE J. Sel. Areas Commun.*, vol. 41, no. 9, pp. 2729–2750, Sep. 2023.

[2] M. Mohammadi et al., "A comprehensive survey on full-duplex communication: Current solutions, future trends, and open issues," *IEEE Commun. Surveys Tuts.*, vol. 25, no. 4, pp. 2190–2244, 4th quart., 2023.

[3] M. Elsayed et al., "Machine learning-based self-interference cancellation for full-duplex radio: Approaches, open challenges, and future research directions," *IEEE Open J. Veh. Technol.*, vol. 5, pp. 21–47, Nov. 2023.

[4] M. Elsayed et al., "Low complexity neural network structures for self-interference cancellation in full-duplex radio," *IEEE Commun. Lett.*, vol. 25, no. 1, pp. 181–185, Jan. 2021.

[5] M. Elsayed et al., "Hybrid-layers neural network architectures for modeling the self-interference in full-duplex systems," *IEEE Trans. Veh Technol.*, vol. 71, no. 6, pp. 6291–6307, Jun. 2022.

[6] M. Elsayed et al., "Full-duplex self-interference cancellation using dual-neurons neural networks," *IEEE Commun. Lett.*, vol. 26, no. 3, pp. 557–561, Mar. 2022.

[7] Y. Kurzo et. al., "Hardware implementation of neural self-interference cancellation," *IEEE J. Emerg. Sel. Topics Circuits Syst.*, vol. 10, no. 2, pp. 204–216, Jun. 2020.

[8] C. Auer et. al., "Support vector machines for self-interference cancellation in mobile communication transceivers," in *Proc. IEEE Veh. Technol. Conf.*, June 2020, pp. 1–6.

[9] M. Erdem et. al., "Nonlinear digital self- interference cancellation with SVR for full duplex communication," in *Proc. IEEE Wireless Commun. Netw. Conf.*, June 2020, pp. 1–6.

[10] M. Yilan et. al., "Integrated linear and nonlinear digital cancellation for full duplex communication," *IEEE Wireless Commun.*, vol. 28, no. 1, pp. 20–27, Feb. 2021.

[11] P.-H. Wang, J.-H. Chen, Y.-Y. Yang, C. Lee, and Y. J. Tseng, "Recent advances in quantum computing for drug discovery and development," *IEEE Nanotechnol. Mag.*, vol. 17, no. 2, pp. 26–30, Apr. 2023.

[12] T. Q. Duong et al., "Quantum-inspired machine learning for 6G: Fundamentals, security, resource allocations, challenges, and future research directions," *IEEE Open J. Veh. Technol.*, vol. 3, pp. 375-387, Aug. 2022.

[13] A. Paul et al., "Quantum-enhanced DRL optimization for DoA estimation and task offloading in ISAC systems," *IEEE J. Sel. Areas Commun.*, vol. 43, no. 1, pp. 364–381, Sep. 2024.

[14] A. Alsaui, I. Al-Nahhal, and O. A. Dobre, "When are quantum algorithms applicable for signal decoding in wireless communication?," *IEEE Open J. Commun. Soc.*, vol. 5, pp. 6314–6328, Sept. 2024.

[15] M. Elsayed and O. A. Dobre, "A Hybrid quantum-classical machine learning approach for self-interference cancellation in full-duplex transceivers," *IEEE Commun. Lett.*, early access, Feb. 2025.

[16] V. Havlíček et al., "Supervised learning with quantum enhanced feature spaces," *Nature*, vol. 567, no. 7747, pp. 209–212, Mar. 2019.

[17] F. Z. Ruskanda et al., "Quantum-enhanced support vector machine for sentiment classification," *IEEE Access*, vol. 11, pp. 87520–87532, Aug. 2023.